JGR Oceans

RESEARCH ARTICLE

10.1029/2023JC020661

A Laboratory Study of the Effects of Size, Density, and Shape on the Wave-Induced Transport of Floating Marine Litter

R. Calvert[1,2], A. Peytavin[3], Y. Pham[3], A. Duhamel[3], J. van der Zanden[4], S. M. van Essen[4,5], B. Sainte-Rose[3], and T. S. van den Bremer[2,6]

[1]School of Engineering, University of Edinburgh, Edinburgh, UK, [2]Faculty of Civil Engineering and Geosciences, Delft University of Technology, Delft, The Netherlands, [3]The Ocean Cleanup Foundation, Rotterdam, The Netherlands, [4]Maritime Research Institute Netherlands, Wageningen, The Netherlands, [5]Faculty of Mechanical, Maritime and Materials Engineering, Delft University of Technology, Delft, The Netherlands, [6]Department of Engineering Science, University of Oxford, Oxford, UK

Abstract Floating marine litter is transported by several mechanisms, including surface waves. In studies of marine litter transport, the wave-induced drift is set to be equal to the Stokes drift, corresponding to the Lagrangian-mean wave-induced drift of an infinitesimally small tracer. Large-scale experiments are used to show how the wave-induced drift of objects of finite size depends on their size, density, and shape. We observe increases in drift of 95% compared to Stokes drift for discs with diameters of 13% of the wavelength, up to 23% for spheres with diameters of 3% of the wavelength, whereas drift is reduced for objects that become submerged such as nets. We investigate what these findings may imply for the transport of plastic pollution in realistic wave conditions and we predict an increase in wave-induced drift for (very) large plastic pollution objects. The different extrapolation techniques we explore to make this prediction exhibit a large range of uncertainty.

Plain Language Summary In transport models for floating marine litter, surface wave effects are often included by simply superimposing their Stokes drift (the small net drift induced by waves) upon wind-driven flows and currents. However, size and shape can be important factors determining a floating marine litter object's wave-induced drift, which generally increases with object size. Large-scale experiments are used to show how the wave-induced drift of floating marine litter objects of finite size depends on their size, density and shape. We observe increases in drift of 95% compared to Stokes drift for discs with diameters of 13% of the wavelength, up to 23% for spheres with diameters of 3% of the wavelength, whereas drift is reduced for objects that become submerged such as nets. We investigate how these findings may affect the transport of plastic pollution in realistic wave conditions, where we believe there will be an increase in wave-induced transport for (very) large plastic pollution objects, although further research is needed to reduce uncertainty.

Key Points:

- For large objects, size and shape can determine a floating marine litter object's wave-induced drift, which generally increases with size
- Increases in drift of 95% compared to Stokes drift have been observed in experiments for discs with diameters of 13% of the wavelength
- Plastic from the ocean exhibited an increase in drift with size unless objects become submerged, such as nets which had decreased drift

Correspondence to:

T. S. van den Bremer,
t.s.vandenbremer@tudelft.nl

Citation:

Calvert, R., Peytavin, A., Pham, Y., Duhamel, A., van der Zanden, J., van Essen, S. M., et al. (2024). A laboratory study of the effects of size, density, and shape on the wave-induced transport of floating marine litter. *Journal of Geophysical Research: Oceans*, *129*, e2023JC020661. https://doi.org/10.1029/2023JC020661

Received 20 NOV 2023
Accepted 21 JUN 2024

Author Contributions:

Conceptualization: R. Calvert, B. Sainte-Rose, T. S. van den Bremer
Data curation: R. Calvert, Y. Pham, J. van der Zanden, S. M. van Essen
Formal analysis: R. Calvert
Funding acquisition: T. S. van den Bremer
Investigation: R. Calvert, A. Peytavin, Y. Pham, A. Duhamel, T. S. van den Bremer
Methodology: R. Calvert, T. S. van den Bremer
Project administration: T. S. van den Bremer
Resources: R. Calvert, Y. Pham, J. van der Zanden, B. Sainte-Rose, T. S. van den Bremer
Supervision: J. van der Zanden, S. M. van Essen, B. Sainte-Rose, T. S. van den Bremer

1. Introduction

Floating plastic marine litter has rapidly become one of the most acute environmental problems (Eriksen et al., 2014), particularly affecting marine ecosystems (Lavender Law, 2017). The total oceanic plastic budget is poorly understood. A significant mismatch exists between the estimated amount of land-generated plastic entering coastal waters (5–12 million tonnes yr^{-1}, Jambeck et al., 2015) and the estimated total amount of plastic floating at sea (less than 0.3 million tonnes, Cózar et al., 2014; Eriksen et al., 2014; van Sebille et al., 2015). Similarly, the amount of plastics measured at sea (Lebreton et al., 2019; Ostle et al., 2019; Wilcox et al., 2020) has not kept pace with growth in global plastic production (Geyer et al., 2017; Goldstein et al., 2012). To understand this mismatch, an improved understanding of the physical processes governing transport and dispersion is required (Kaandorp et al., 2023; van Sebille et al., 2020).

As a particle undergoes its periodic motion beneath surface waves, it experiences a Lagrangian-mean velocity in the waves' direction known as Stokes drift (Stokes, 1847). Stokes drift is the difference between the Lagrangian-mean velocity of a fluid parcel and the Eulerian-mean velocity of the fluid measured at a fixed spatial location (e.g., Bühler, 2014; van den Bremer & Breivik, 2017). At any time and location on the open ocean, the wave field is a superposition of waves that have been generated by earlier winds at another location. Wave models, such as WAM (The WAMDI Group, 1988) and WaveWatch-III (Tolman, 2009), have been developed to predict wave fields and thus Stokes drift (Breivik, Janssen, & Bidlot, 2014; Webb & Fox-Kemper, 2011). Recently, Lenain and

Validation: R. Calvert
Writing – original draft: R. Calvert
Writing – review & editing: R. Calvert, T. S. van den Bremer

Pizzo (2020) have shown that up to 50% of the Stokes drift can result from high-frequency terms in the wave spectrum, which are often not resolved in models nor measured by wave buoys.

A recent and growing body of literature is examining the role of Stokes drift in the transport and dispersion of floating plastic pollution. Iwasaki et al. (2017) showed that in the Sea of Japan, Stokes drift pushed micro-plastics closer to the coast. Delandmeter and van Sebille (2019) and Onink et al. (2019) report a similar result in Arctic regions. Dobler et al. (2019) demonstrated that Stokes drift fundamentally changes transport patterns in the South Indian Ocean by shifting the convergence regions to the west, causing leakage into the South Atlantic rather than the South Pacific. Stokes drift may also allow particles to cross strong circumpolar winds and currents (Fraser et al., 2018).

Importantly, the aforementioned studies have simply superimposed the Stokes drift onto the Eulerian current field obtained from ocean general circulation models or observations. There are three important limitations to this. First, it ignores the fact that the Eulerian flow is itself modified by surface waves: on the rotating Earth, the Coriolis force associated with the Stokes drift drives an Eulerian-mean current in the turbulent upper-ocean boundary layer. This so-called Ekman—Stokes flow needs to be added to the Stokes drift to properly estimate the wave-induced Lagrangian-mean flow which transports floating marine litter (Higgins et al., 2020). Second, the drift at the surface of a breaking wave is much larger than the prediction of classical Stokes drift (Deike et al., 2017), as confirmed in experiments (Lenain et al., 2019; Sinnis et al., 2021), and breaking may make a significant contribution to the Lagrangian drift of realistic wave fields (Pizzo et al., 2019). Eeltink et al. (2023) created a stochastic model for drift in breaking waves in realistic spectral seas; the predictions were then compared to large basin experiments. Third, a finite-size floating object with a different density to water will behave very differently from an infinitesimally small, perfectly Lagrangian tracer, as considered hitherto, and this too will have an effect on its wave-induced transport, which is the focus of this paper. In their perspective, Sutherland et al. (2023) note that the Reynolds and Stokes numbers of plastic pollution objects in the ocean are neither large nor small, limits in which most research has previously been conducted. This makes understanding the effect of object size, density, and shape on floating marine litter transport in wavy free-surface flows particularly challenging (Sutherland et al., 2023), motivating the present study.

Focusing on fully submerged particles, Eames (2008) and Santamaria et al. (2013) used the Maxey–Riley equations (Maxey & Riley, 1983) to examine how far slightly positively or negatively buoyant objects are transported by regular waves as they either rise to the free surface or sink. Santamaria et al. (2013) predicted that positively buoyant objects in deep-water waves experience an increase in drift owing to their inertia (see DiBenedetto et al. (2022) for an extension to finite depth). Also considering fully submerged objects, DiBenedetto and Ouellette (2018) showed that non-spherical objects have a preferential orientation under waves, confirming this result numerically (DiBenedetto & Ouellette, 2018) and experimentally (DiBenedetto et al., 2019), but not examining the effect of the object's inertia or its modified drift. Even without direct modification of the drift, the orientation changes the drag on slightly negatively buoyant objects, which results in objects of different shapes being transported different distances before "raining out" (DiBenedetto et al., 2018). Taking a similar approach, Pujara and Thiffeault (2023) have shown that wave action reduces the vertical dispersion of particles but increases horizontal dispersion.

For floating discs, experiments by Huang et al. (2016) showed a significant increase in wave-induced transport compared to Stokes drift (in non-breaking waves). Alsina et al. (2020), on the other hand, observed no change in transport compared to Stokes drift, but only considered spheres with a maximum diameter of 0.6% of the wavelength. This paper is an extension of that study, considering larger objects and a range of shapes and densities. Through a combination of theory and exploratory experiments for idealized spherical objects in deep-water waves, Calvert et al. (2021) showed that different floating objects are transported at different rates depending on their size and density, and that larger buoyant objects can have increased drift compared with Lagrangian tracers. Calvert et al. (2021) found that the predominant driver for increased drift is the object size relative to wavelength, with an estimated doubling of the wave-induced drift for spheres with a diameter of 6% of the wavelength. Xiao et al. (2024) identified a mechanism known as the diffraction-modified Stokes drift, by which the drift of relatively large objects (~10% of the wavelength) can be enhanced and found good agreement with numerical simulations.

To characterize the effects of size, density and shape on the wave-induced transport of floating marine litter in deep water, we conduct a large-scale experimental campaign in a 220 m long wave basin. We measure the drift of

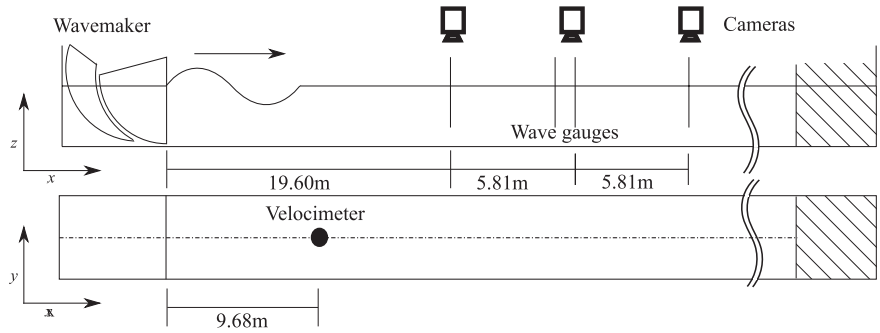

Figure 1. Experimental set-up and measurement devices.

28 different objects, a number of which are real marine litter samples, and 7 deep-water wave conditions representative of conditions in the Great Pacific Garbage Patch, obtaining a total of more than 1,500 object drift trajectories. This paper reports these results, proposes a parametrization to be used in future studies of marine litter transport, and estimates the implications for wave-induced drift of different-size marine litter objects in the Great Pacific Garbage Patch.

2. Experimental Methodology

2.1. Set-Up and Data Acquisition

Experiments were carried out in the Concept Basin at the Maritime Research Institute Netherlands (MARIN). Figure 1 shows a diagram of the set-up and the locations of the different measurement devices. The basin had length of 220 m, width of 4 m and still-water depth of 3.6 m. Regular waves were generated by multiple hinged flap-type wave-makers.

Waves were allowed to travel the length of the flume until being absorbed by a beach. The wave paddle was controlled with a second-order signal. Four resistance-type wave gauges sampled the free surface along the basin at 200 Hz, and Eulerian current measurements were taken using a NOBSKA velocimeter at 100 Hz suspended from a gantry at a fixed height and location. Three full-HD Marshall CV502-WPM cameras captured the movement of the floating objects at 25 frames per second (fps) using a 1/50 s shutter speed from their ceiling-mounted positions. Objects were released by hand a short distance before the start of the camera section and removed a short distance afterward. In between, the objects experienced continuously generated regular wave motion. Objects were released close to the center-line of the basin, where they generally stayed; objects with trajectories moving into vicinity of the basin side-walls were not considered in the analysis.

The objects were tracked from the ceiling-mounted cameras using the CRST algorithm (Lukezic et al., 2017) over a 7.5 by 4.5 m window aligned with the flume direction. The trajectories were undistorted and calibrated into the physical plane of the still-water surface by inverting the transformation matrix iteratively, where the transformation matrix was calculated using a series of images of a 100 mm square calibration grid floated on the free surface using MATLAB's Camera Calibration toolbox (Zhang, 2000). The horizontal motion was low-pass filtered at $0.5f$, with f the regular-wave frequency, to extract the object's mean drift $\overline{u}_O$, which was calculated as the gradient of a fitted linear line to this sub-harmonic motion. Significant lateral motion was only observed for steeper waves, where the wave field became subject to instabilities (cross modes) in the direction normal to wave propagation (y). In the rest of the paper, only the motion in the direction of wave propagation is considered. Each trajectory was inspected manually to ensure the object's drift velocity had reached a steady state and that the fit was accurate before a mean and standard deviation were calculated from 8 repeated experiments.

2.2. Wave Conditions

Experiments were carried out for 7 regular wave conditions as shown in Table 1, with the three non-dimensional water depths representative of the deep ocean ($kd > 3$ with $k = 2\pi/\lambda$ the wavenumber, λ the wavelength, and $d = 3.6$ m the depth of the basin). As deep-water waves were chosen to represent the ocean, the effects of bottom

Table 1
Matrix of the 7 Wave Conditions Used, Listing: Measured Frequency f; Wavenumber $k = \omega^2/g$ With $\omega = 2\pi f$ and g the Gravitational Acceleration; Measured Wave Amplitude a, Where the Standard Deviation Is of the Amplitude Envelope Over the Duration of an Experiment; Steepness $\epsilon = ka$, and Predicted Average Stokes Drift at the Still-Water Level ($z = 0$) $u_S = c\,\epsilon^2$ With $c = \omega/k$, Where the Standard Deviation Results From the Variability in the Amplitude Envelope Over the Duration of an Experiment

Wave condition	f (Hz)	k (1/m)	kd (−)	a (mm)	$\epsilon = ka$ (−)	$\overline{u}_S$ (mm/s)
1	1.00	4.02	14.5	39 ± 1	0.159	39 ± 2
2	1.00	4.02	14.5	68 ± 2	0.275	118 ± 6
3	1.00	4.02	14.5	78 ± 8	0.316	157 ± 30
4	0.50	1.01	3.6	150 ± 5	0.154	74 ± 5
5	0.50	1.01	3.6	230 ± 7	0.270	226 ± 11
6	0.50	1.01	3.6	110 ± 1	0.115	42 ± 1
7	0.67	1.80	6.5	210 ± 10	0.380	338 ± 32

friction can evidently be neglected. The flap-type wavemaker can generate up to a period of 1 s. The range of steepnesses $\epsilon = ka$, with a the wave amplitude, $\epsilon = 0.12$–0.38, were chosen to correspond to low, medium and high-steepness cases, with significant wave breaking in the high-steepness case. The (linearized) amplitudes in Table 1 are obtained by frequency filtering the measured surface elevation between $0.8f$ and $1.2f$, thus removing nonlinear (bound) waves at these lower and higher frequencies and retaining an (approximately) linear surface elevation.

2.3. Floating Marine Litter Objects

Experiments were carried out for a total of 28 floating objects in two categories: (I) idealized objects and (II) realistic marine litter objects. Object characteristics are shown in Table 2. Object size was captured by making the object's characteristic size D (e.g., the diameter) non-dimensional by the wavelength, that is, $\delta = D/\lambda$ (following Calvert et al. (2021)), allowing relative object size to be varied by changing object size or wavelength. The object size relative to wavelength was restricted by the wave-generating capabilities and available object sizes. Object density was obtained by directly measuring the mass by weighing each object and subsequently inferring the volume displaced by the object by measuring the submerged mass of the object. Object density is captured by the density ratio $\beta = \rho_O/\rho_w$, where ρ_O and ρ_w are the densities of the object and water, respectively.

The category of idealized objects (I) consists of 15 spheres of 4 different diameters and a range of densities and 4 discs of 4 different diameters, each with a thickness of 2.5 cm, with dimensional and non-dimensional object properties summarized in Table 2 (see Table A1 for a detailed list of idealized object properties). The range of relative sizes in our experiments ($0.3\% < \delta < 3.2\%$ for spheres and $0.8\% < \delta < 13\%$ for discs) and relative densities ($0.20 < \beta < 0.92$ for the spheres) aims to capture the full range of values for marine litter objects found in the Great Pacific Garbage Patch (e.g., Lebreton et al., 2018). The lower bound of relative size in our experiments is chosen to correspond to the Lagrangian limit, in which drift is not enhanced compared to the Stokes drift; the relatively large upper bound has been chosen to allow clear observation of enhanced wave-induced drift in our experiments. The category of realistic marine litter objects (II) includes bottle caps, a tray, a cable guide, elongated plates and three different fishing nets that were collected from the Great Pacific Garbage Patch.

2.4. Accounting for Wave-Induced Eulerian Flows

Wave-induced Eulerian-mean flows have resulted in considerable difficulty observing Stokes drift in laboratory wave flumes, as the behavior of these Eulerian-mean flows is hard to predict (see reviews by van den Bremer & Breivik (2017) and Monismith (2020)). These Eulerian-mean flows are initially irrotational but will change over time, as vorticity is advected (by the mean flow itself) from the wavemaker or the beach and may be unstable (Longuet-Higgins, 1953). As Eulerian-mean flows are specific to a laboratory flume (and very different to the real ocean), and may even vary in time during an experiment, we would like to eliminate their effect on object drift. To do so, we use two methods. Elimination of the Eulerian-mean flow requires either direct measurement of the Eulerian current in the flume (Method 1) or inference of the Lagrangian velocity of an infinitesimally small object

Table 2
Description and Shape, Parameter Range and Observed Behavior for Idealized Objects (Category I, Object No. 1–19) and Realistic Marine Litter Objects (Category II, Object No. 20–28)

No.	Picture	Description and shape	D (mm)	ρ_O (kg/m^3)	$\delta = D/\lambda$ (%)	$\beta = \frac{\rho_O}{\rho_w}$	F/S	$\chi = \frac{\overline{u}_O - \overline{u}_E}{u_S}$
1–15		Spheres	20–50	195–920	0.32–3.2	0.20–0.92	F	1.03–1.23
16–19		Discs	50–200	750–880	0.8–12.8	0.75–0.88	F	1.00–1.95
20		Small bottle cap	30	965	0.48–1.92	0.97	F	1.16 ± 0.08
								1.30 ± 0.14
21		Large bottle cap	60	896	0.96–3.84	0.90	F	1.09 ± 0.05
								1.34 ± 0.04
22		Medium tray	130	998	2.08–8.32	1.0	F	1.12 ± 0.05
								1.62 ± 0.18
23		Cable guide	112	941	1.80–7.19	0.94	F	1.18 ± 0.18
								1.40 ± 0.09
24		Long plate (1)	225	992	3.60–14.44	0.99	F	1.20 ± 0.18
								1.33 ± 0.08
25		Long plate (2)	255	969	4.08–16.33	0.97	F	1.19 ± 0.11
								1.61 ± 0.10
26		Coarse net fragment	300	990	4.8–19.2	0.99	S	0.59 ± 0.02
								0.68 ± 0.07
27		Fine net fragment	200	995	3.2–12.8	1.0	S	0.57 ± 0.11
								0.81 ± 0.09
28		Fine square net	300	979	4.8–19.2	0.98	S	0.91 ± 0.07
								1.1 ± 0.15

Note. The largest length scale is chosen as the characteristic scale D. Object density ρ_O is estimated by hydrostatic weighing. The observed behavior of objects can be either floating on the surface (F) or suspended below the surface (S). The drift enhancement factor χ is calculated as the ratio of the measured mean drift of the object $\overline{u}_O$ minus the Eulerian-mean speed $\overline{u}_E$ normalized by the predicted Stokes drift u_S, that is, $\chi \equiv (\overline{u}_O - \overline{u}_E)/u_S$ (using Method 2). For idealized objects (category I), the range of χ values obtained is shown, whereas for realistic marine litter objects (category II) values of χ are shown for the wave conditions resulting in the smallest and the largest relative size.

from the transport of finite-size objects (Method 2). Neither method is perfect, and we discuss their advantages and disadvantages below.

2.4.1. Method 1: Measured Eulerian Current

Eulerian current measurements were taken using a NOBSKA velocimeter that is always submerged. Measurements from the velocimeter are dominated by the periodic linear wave velocity, which we remove by taking a mean in time over the duration of each experiment. The Eulerian-mean velocities at a small depth below the free surface are shown for each wave condition in Table 3, where the mean and both the standard deviation obtained from repeats and the standard deviation obtained from variation of the Eulerian-mean velocity in time are shown. It is evident from Table 3 that these variations in the Eulerian-mean flow (both from variations in time and from repeated experiments) are small enough not to significantly affect our results. Using Method 1, the drift enhancement factor for each repeated experiment of each object can then be calculated as $\chi = (\overline{u}_O - \overline{u}_E)/u_S$, where $\overline{u}_O$ is the mean object drift speed we measure, $\overline{u}_E$ is the Eulerian-mean speed of the fluid, and $u_S = \epsilon^2\omega/k$ is the Stokes drift. The drift enhancement factor χ is then averaged over repeated experiments to give a single value for each object and each wave condition. The Lagrangian-mean speed $\overline{u}_L$ is equal to the sum of the Stokes drift u_S and the Eulerian-mean speed $\overline{u}_E$ by definition.

2.4.2. Method 2: Inferred Lagrangian Velocity

Method 2 infers the Lagrangian velocity of an infinitely small object by fitting to the object velocities of the four discs, averaging over repeated experiments, and then extrapolating the fit to a zero-diameter disc, with fits shown

Table 3
Measured (Method 1) and Inferred (Method 2) Eulerian-Mean and Lagrangian-Mean Velocities, Where the Lagrangian-Mean Velocity Is Obtained by Adding the Predicted Stokes Drift to the Measured Eulerian-Mean Velocity (Method 1), and the Eulerian-Mean Velocity Is Obtained by Subtracting the Predicted Stokes Drift From the Lagrangian-Mean Velocity (Method 2)

Wave condition	$\overline{u}_E$(mm/s) Method 1	$\overline{u}_E$(mm/s) Method 2	$\overline{u}_L$(mm/s) Method 1	$\overline{u}_L$(mm/s) Method 2
1	−3 ± 1, 1	−11	36 ± 2	28 ± 5
2	−10 ± 2, 2	−17	108 ± 6	101 ± 11
3	−11 ± 4, 6	−17	146 ± 30	140 ± 27
4	−6 ± 9, 2	−27	68 ± 5	47 ± 9
5	−78 ± 2, 5	−105	148 ± 11	121 ± 9
6	−3 ± 1, 1	−6	39 ± 1	36 ± 4
7	−21 ± 1, 2	2	317 ± 32	340 ± 47

Note. For $\overline{u}_E$, the first standard deviation for Method 1 is of the time-averaged velocity over repeated experiments and the second standard deviation for Method 1 is the average over repeated experiments of the standard deviation from variation in time over the duration of each experiment; no standard deviation is reported for Method 2. For $\overline{u}_L$, using Method 1, the standard deviation is the square root of the sum (assuming independence) of the first standard deviations of $\overline{u}_E$ squared and the standard deviation in the Stokes drift from variation in amplitude squared (Stokes drift variation is reported in Table 1). The standard deviation of $\overline{u}_L$, for Method 2 is the one associated with the fit (cf. Figure 2).

for the 7 wave conditions in Figure 2. The difference between the inferred velocity of a zero-diameter disc and the predicted Stokes drift is the Eulerian-mean velocity at the surface: $\overline{u}_E = \overline{u}_{O,D\to 0} - u_S$ for each wave condition. The drift enhancement factor is then calculated using the inferred Eulerian-mean velocity at the surface.

2.4.3. Comparison of Method 1 and Method 2

Figure 3 confirms a very high degree of correlation between the values of the Eulerian-mean and the Lagrangian-mean velocities obtained using Method 1 and Method 2 (N.B. the better visual agreement for the Lagrangian-mean velocities in Figure 3b than for the Eulerian-mean velocities in Figure 3b is due to the relatively large contribution of the Stokes drift compared to the Eulerian-mean flow). Figure 3a suggests that the Eulerian-mean velocity obtained using Method 2 (at the surface) is generally larger in magnitude (i.e., more negative) then the Eulerian-mean velocity obtained using Method 1 (at depth). As a result, Method 1 will generally result in smaller values of the drift enhancement factor. We will discuss the effect this has on our results in Section 3.

3. Results

The objective of this paper is to examine the effects of size, density and shape on the wave-induced transport of floating marine litter. To do so, we introduce a drift enhancement factor $\chi \equiv (\overline{u}_O - \overline{u}_E)/u_S$, where $\overline{u}_O$ is the mean object drift speed we measure, $\overline{u}_E$ is the Eulerian-mean speed of the fluid, and u_S is the Stokes drift, which an infinitesimally small, perfectly Lagrangian tracer would experience in a wave field in the absence of Eulerian-mean flows. The drift enhancement factor χ thus measures the ratio of object drift to Stokes drift, both in the absence of Eulerian-mean flows, with $\chi = 1$ corresponding to no drift enhancement.

In order to investigate and eliminate Eulerian-mean flows we use two different methods. Method 1 makes use of the Eulerian-mean flow measurements we have taken below the surface (it is not possible to measure the Eulerian-

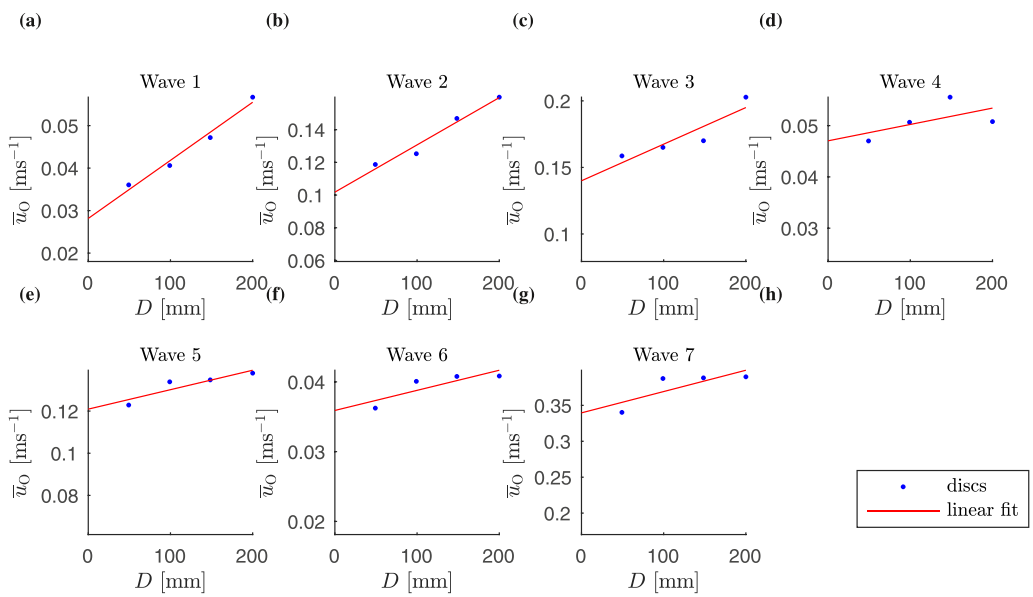

Figure 2. Linear fits used to calculate the Lagrangian velocity at the free surface in Method 2. The linear fit of the object drift velocity $\overline{u}_O$ as a function of disc diameter D is shown in each panel for the 7 wave conditions.

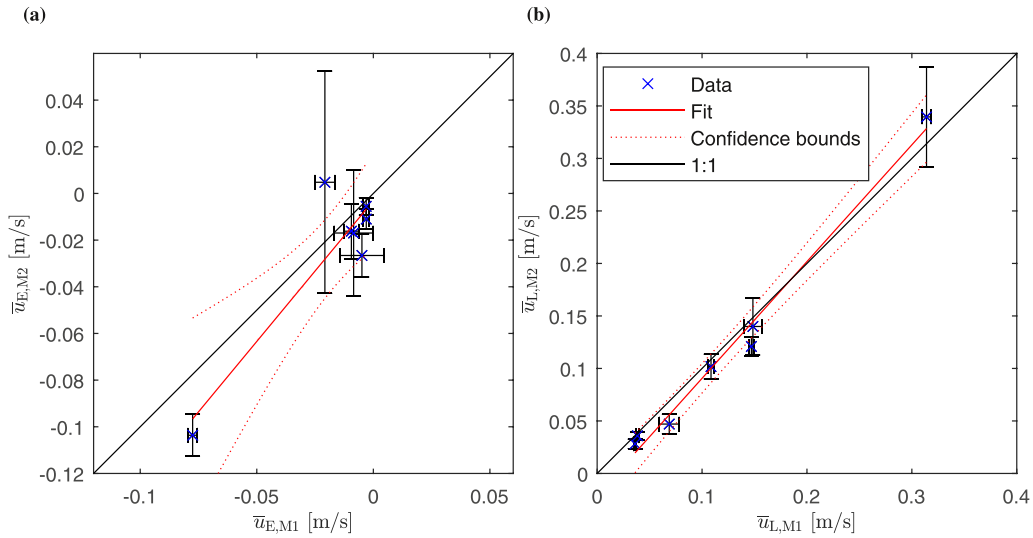

Figure 3. Comparison of the Eulerian-mean (a) and the Lagrangian-mean (b) velocity between Method 1, which measures the Eulerian-mean velocity at depth ($\overline{u}_{E,M1}$, $\overline{u}_{L,\,M1}$), and Method 2, which infers the Lagrangian-mean velocity at the surface from a fit ($\overline{u}_{L,\,M2}$, $\overline{u}_{L,\,M2}$). The error bars are one standard deviation either side of the mean for each wave condition, where the standard deviation is over repeated experiments for Method 1 and the error associated with the fit for Method 2.

mean flow at the surface). Consequently, Method 1 cannot guarantee that $\chi = 1$ for an infinitely small, perfectly Lagrangian tracer at the surface. In Method 2, $\chi = 1$ by assumption for an infinitely small, perfectly Lagrangian tracer, which we obtain from extrapolation (to $D = 0$) of the measured relationship between object drift speed and relative size for discs. Drift enhancement of other objects is measured relative to this case in Method 2. We choose Method 2 for the estimation of drift enhancement factors in Table 2 because the intercept γ_0 is close to unity; both Methods are used for the quantitative analysis of the effects of size and density in Section 3.1.

Table 2 reports the values of the drift enhancement factor χ we have obtained from our experiments. For idealized objects (no. 1–19), only the range of explored relative size (δ) and relative density (β) and observed χ values are reported, with the relationship examined in more detail in Section 3.1. For realistic marine litter objects (no. 20–28), only the cases with the smallest and largest relative size (δ) are shown in Table 2, with corresponding values of χ and their standard deviations (from repeated experiments).

3.1. Idealized Objects (Category I)

To identify the effects of relative size, $\delta = D/\lambda$, and relative density, $\beta = \rho_O/\rho_w$, in our experimental data for idealized objects (Category I), we perform the following linear regression for the drift enhancement factor χ:

$$\chi = \gamma_0 + \gamma_\delta \delta + \gamma_\epsilon \epsilon + \gamma_\beta \beta, \tag{1}$$

where an additional dependence on steepness $\epsilon = ka$ is included to accommodate the potential effects of breaking-induced drift enhancement in the higher-steepness cases (cf. Deike et al., 2017; Lenain et al., 2019; Sinnis et al., 2021).

Table 4 shows the values of the coefficients in Equation 1 we obtain. Figure 4 (discs) and Figure 5 (spheres) show the regressions graphically. For discs, we have first considered the different wave conditions grouped according to steepness before considering all wave conditions together. For spheres, we only show results for the medium-steepness case. For the low-steepness case, the small value of drift makes it more difficult to estimate this from the experiments, especially for lighter spheres, which can be affected by air flows and small cross-modes in the wave field, resulting in a large number of spheres leaving the field of view and excessive measurement error. For the high-steepness case, tracking of the smaller spheres became too difficult due to breaking waves.

Table 4
Dependence of the Drift Enhancement Factor χ on Relative Size, $\delta = D/\lambda$, Relative Density, $\beta = \rho_O/\rho_w$, and Steepness, $\epsilon = ka$ According to Linear Regression (1) for Idealized Objects (Category I) Distinguishing the Different Wave Conditions From Table 1 Grouped According to Steepness

Object (No.)	Steepness	Wave conditions	M1 M2	γ_0	γ_δ	γ_ϵ	$\gamma_\beta \times 10^5$	R^2
Spheres (1–15)	Medium	2 and 5	M1	0.78 ± 0.05	11.2 ± 1.0	–	0.59 ± 6.4	0.73
			M2	1.11 ± 0.02	2.8 ± 0.5		−2.9 ± 2.4	0.54
Discs (16–19)	Low	1 and 4	M1	0.86 ± 0.027	4.6 ± 0.4	–	–	0.95
			M2	0.94 ± 0.034	8.1 ± 0.6			0.96
	Medium	2 and 5	M1	0.74 ± 0.050	5.7 ± 0.8	–	–	0.90
			M2	1.00 ± 0.017	4.4 ± 0.3			0.97
	High	3 and 7	M1	1.06 ± 0.094	5.6 ± 1.3	–	–	0.73
			M2	1.02 ± 0.043	4.3 ± 0.6			0.78
	All	1–7	M1	0.62 ± 0.11	5.6 ± 0.8	0.94 ± 0.38	–	0.73
			M2	1.20 ± 0.08	5.3 ± 0.5	−0.83 ± 0.26		0.82

Note. The two rows for each case (M1/M2) correspond to Method 1 and Method 2 for eliminating the Eulerian-mean current. The error bands correspond to ±the standard deviation, and R^2 is the coefficient of determination of the fit to the data.

3.1.1. Effects of Size and Density

For both spheres and discs there is clear evidence of the drift enhancement factor χ increasing with relative object size δ. There is significant uncertainty in the value of γ_δ for spheres, varying significantly between Method 1 and 2. This relationship is more robust for discs (larger γ_δ), for which it is relatively independent of steepness. As a rule of thumb, the drift enhancement factor goes up by 3% points for spheres and by 5–6 percentage points for discs when their relative sizes go up by 1% point. Discs are thus generally transported faster than spheres. The values in Table 4 are based on data that captures the full range of relative sizes of marine litter objects found in the Great Pacific Garbage Patch (e.g., Lebreton et al., 2018), but the linear relationship with relative size of course becomes invalid for very large relative size. We do not find a significant effect of the relative density β on the drift enhancement factor χ based on the spheres, for which we were able to vary density systematically by using hollow and filled spheres with different ratios of epoxy and glass microspheres, even though the draft varied from 1/3 to 3/4 of the sphere diameter.

For both spheres and discs we find intercept values (γ_0) below 1 using Method 1, suggesting that a perfectly Lagrangian tracer would travel at a reduced speed compared to the Stokes drift (i.e., $\chi < 1$ for $\delta \to 0$). We emphasize that this is likely a result of the (generally negative) wave-induced Eulerian velocity at the surface being much larger (i.e., more negative) than the value measured by the velocimeter.

By comparing the top and bottom row(s) of panels in Figures 4 and 5, which correspond to Methods 1 and 2 respectively, and examining the two sets of coefficients in Table 5, the differences between the two methods of estimating the Eulerian-mean velocity becomes clear. The values of the intercept γ_0 are generally smaller for Method 1, and the values of γ_δ for discs are generally comparable for both methods. The data is generally much less unequivocal for spheres than for discs. There is a significant variation in the value of γ_δ between the two methods for the spheres. This variation is probably explained by the apparent level offset between the three points with the lowest δ (wave condition 5) and the three points with the highest δ (wave condition 2) in Figure 5. This may be caused by the magnitude of the (negative) Eulerian-mean currents at the surface being much larger than what is measured at depth using Method 1 for wave condition 5 (see Table 3). This level offset in χ can also be seen for the discs in the medium-steepness case when using Method 1 in Figure 4 but has less effect on the fitted coefficients because of the larger range of δ values for discs. We therefore suggest using Method 2 for any insight into the drift of spheres.

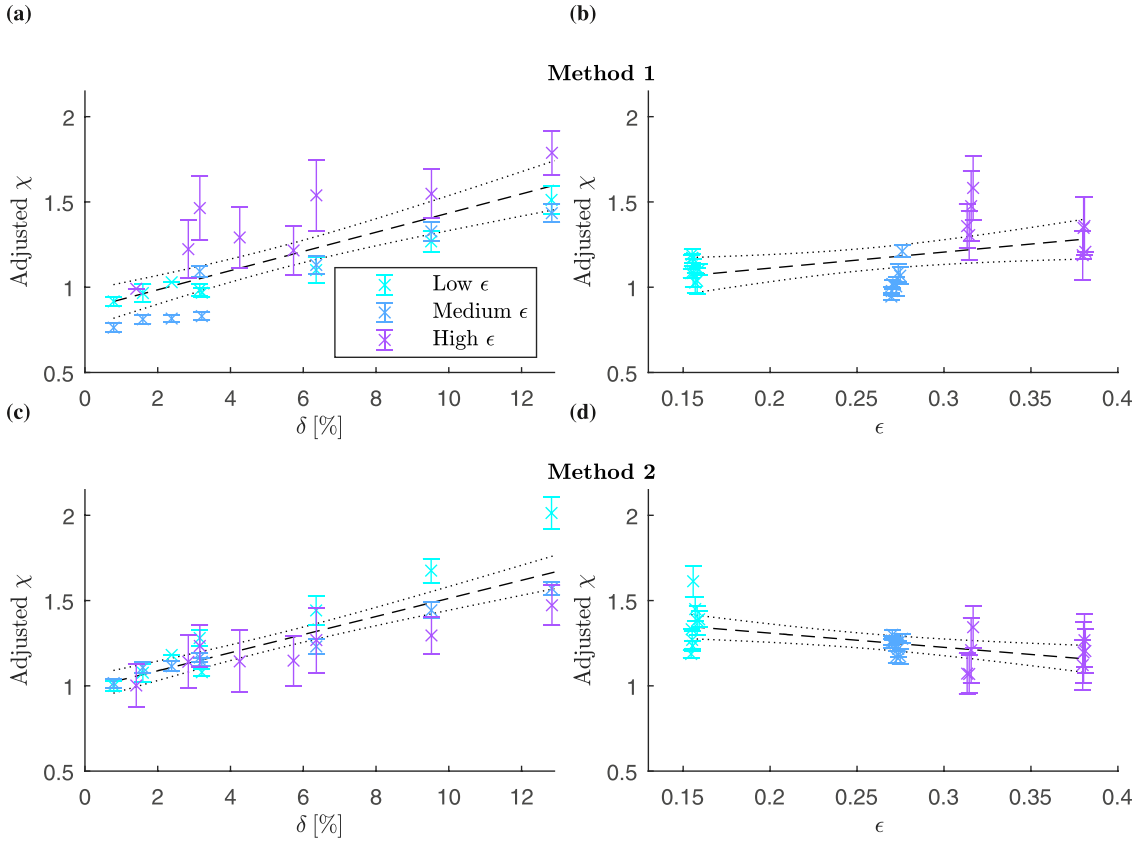

Figure 4. The effects of relative object size δ and wave steepness ϵ on the drift enhancement factor χ for discs calculated from the regression: (a, c) the adjusted drift enhancement factor ($\chi - \gamma_\epsilon \epsilon$) as a function of relative object size δ using Method 1 (a) and Method 2 (c); and (b, d) the adjusted drift enhancement factor ($\chi - \gamma_\delta \delta$) as a function of steepness ϵ using Method 1 (b) and Method 2 (d). Error bars show one standard deviation each side of the mean from repeated experiments. The dashed line shows the best fit and the dotted lines the 95% confidence bands.

3.1.2. Effect of Steepness (and Wave Breaking)

When including all the wave conditions, we find a significant positive linear dependence of the drift enhancement factor χ on the steepness ϵ (using Method 1) for discs (we do not have results pertaining to the effect of steepness for spheres, as explained above). Noting that Method 1 makes use of Eulerian-mean flow velocity measured at depth below the free surface, which is unlikely to increase because of breaking, this additional enhanced drift could be the result of breaking increasing the wave-induced drift at the surface compared to the Stokes drift for larger steepness, as found by Deike et al. (2017), Lenain et al. (2019), and Sinnis et al. (2021). As an alternative hypothesis, part of this additional enhanced drift could be explained by strongly nonlinear boundary-layer streaming (Longuet-Higgins, 1953), as also observed by Grue and Kolaas (2017).

Breaking is captured differently by the two methods. Making the reasonable assumption that breaking will not result in an increase in the Eulerian-mean flow measured by the velocimeter at depth, the increased Lagrangian transport due to breaking will affect all objects and will result in an increased drift enhancement factor χ even for small objects when using Method 1. Indeed, when performing a regression using all wave conditions, we find a positive relationship between χ and ϵ (see Table 5), suggesting steep, breaking waves are associated with greater drift than the Stokes drift as found by Deike et al. (2017), Lenain et al. (2019), and Sinnis et al. (2021) (N.B. that $\chi = \overline{u}_O / u_S$ for $\overline{u}_E = 0$ and $u_S \propto \epsilon^2$). When Method 2 is used, we effectively make the assumption that breaking affects all objects, including Lagrangian tracers, similarly. Breaking is then encapsulated in the inferred value of the Eulerian-mean velocity. The drift enhancement factor χ no longer captures the effect of breaking itself (i.e., $\chi = 1$ in the limit $D \to 0$). When performing a regression using all wave conditions, we find a negative relationship between χ and ϵ (as opposed to the positive relationship for Method 1; see Table 5), suggesting perhaps that breaking reduces the enhancement factor compared to a Lagrangian tracer, by increasing the drift of a Lagrangian

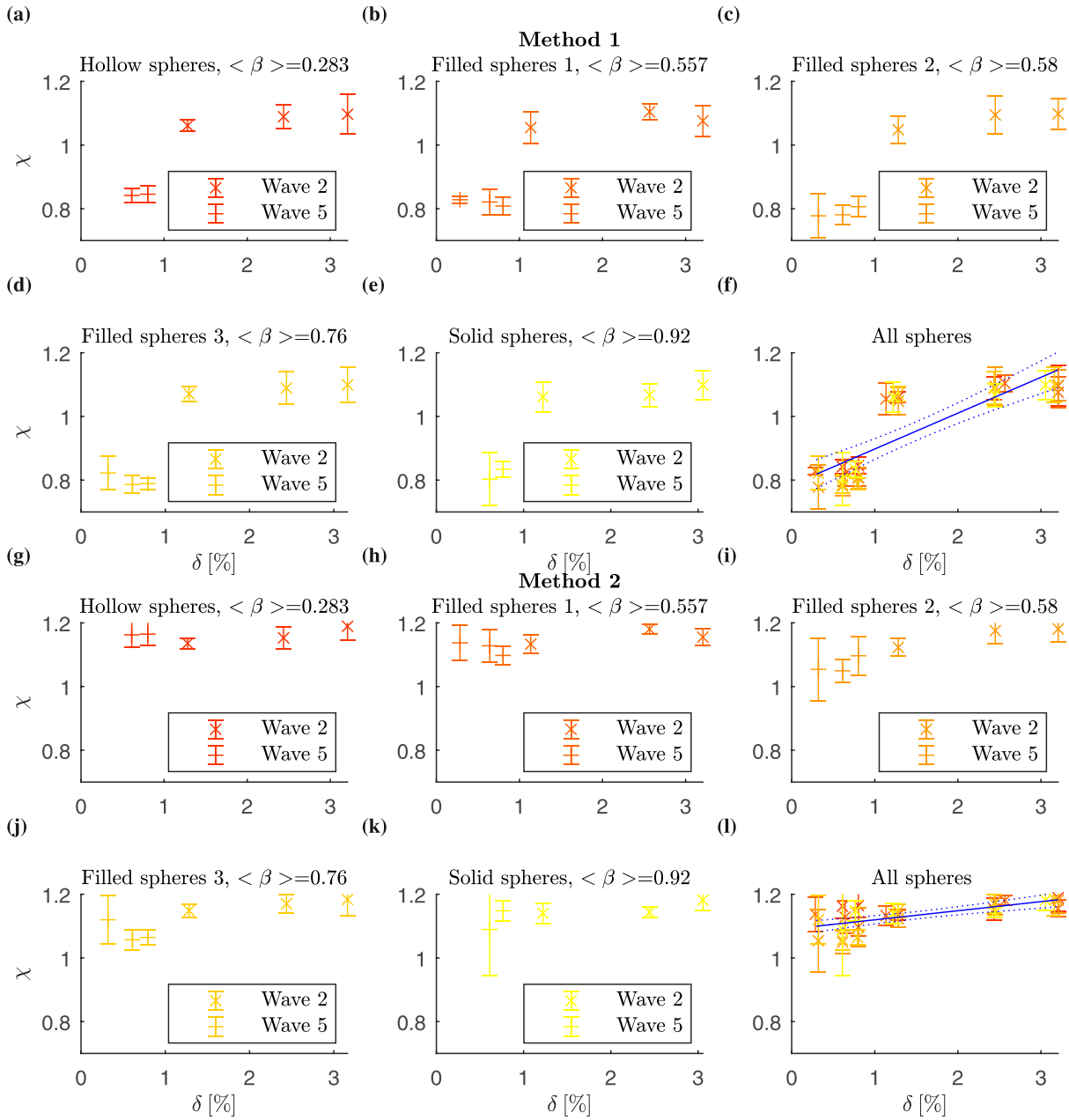

Figure 5. The effects of relative object size δ and wave steepness ϵ on the drift enhancement factor χ for spheres calculated using Method 1 in panels (a)–(f), and Method 2 in panels (g)–(l). The first 5 panels of each method show results for different density spheres with an average object density $<\beta>$ shown above each panel. Error bars show one standard deviation each side of the mean from repeated experiments. Panels (f and l) combine all the data with a linear regression on relative size (blue solid line) and 95% confidence intervals either side. Two different wave conditions (with the same steepness) have been combined for each plot, as shown in the legend. The colors of the markers in panels (f) and (l) correspond to the different densities in the preceding panels.

tracer. In order to draw robust conclusions about the role of steepness and wave breaking, measurements should be made for more than three values of steepness in future work.

3.1.3. Coefficient of Determination

Finally, values of coefficient of determination R^2 for the linear fit shown in Table 4 show that relative size alone can explain the observed variability in drift extremely well for discs in low to medium-steepness waves. However, some unexplained variability remains for spheres, for which our data covers a smaller range of relative sizes, and

Table 5
Predicted Spectrally Weighted Drift Enhancements ($(\chi_{spec,\ A2b} - 1) \times 100\%$) for Floating Marine Litter Objects With Different Sizes Averaged Over a 1-Year Period and in the Case of Maximum (Case 1) and Minimum (Case 2) Drift Enhancement Using Extrapolation Approach 2b

	Object size (cm)	1	10	50	100
1-year average	Mean increase (%)	3	27	51	59
Case 1	Maximum increase (%)	6	47	68	70
Case 2	Minimum increase (%)	2	18	36	43

higher steepness, which would require more than three steepness values to resolve and may require a different dependence on steepness than is included in Equation 1.

3.1.4. Comparison With Theoretical Predictions by Calvert et al. (2021)

For spheres, we can make the comparison with the theoretical model of Calvert et al. (2021) (the theoretical model of Calvert et al. (2021) only considered spheres). Figure 6 shows a reasonable agreement between the experiments and theory for higher density spheres. We have used Method 2 to eliminate the Eulerian-mean flow from the experiments, and the experimental fit has been plotted through ($\delta = 0, \chi = 1$) to enable comparison with theoretical predictions, focusing on the slope of the line. We emphasize that the agreement would be much less good using Method 1 (see Table 4 for the very different slope γ_δ in this case). The theoretical lines are plotted for a range of object densities of 200–800 kg/m^3 ($\beta = 0.2$–0.8) and show a significant dependence on object density, while a significant relationship between the drift enhancement factor and object density could not be identified in experiments (see Table 4). We note higher and lower densities have been excluded, as they violate the assumptions and validity of the perturbation expansion in Calvert et al. (2021). In the diffraction-modified Stokes drift mechanism of Xiao et al. (2024) higher density enhances drift via the greater draft of the objects. It is possible that the limited range of relative sizes of the spheres in our experiments may be the cause of the effect of density being insignificant in our data. This should be examined further by obtaining more data before robust conclusions can be drawn.

3.2. Realistic Marine Litter (Category II)

Taking their longest length scale as the characteristic size D and reporting for the wave conditions resulting in the smallest and the largest relative size $\delta = D/\lambda$, Table 2 reports the drift enhancement factor χ for the 9 realistic marine litter objects (Category II) as well as their standard deviations from repeated experiments. For all realistic marine litter objects, the drift enhancement factor was generally larger for larger relative size, which was achieved by changing the wavelength; this confirms the generality of the result obtained for idealized objects (Category I). We examine the more detailed behavior of each realistic marine litter object in turn.

The small and large bottle caps both experience clear increases in drift with values of the drift enhancement factor even exceeding those for discs of similar relative size. The same holds for the medium tray and the cable guide, which have plate-like geometries similar to a disc. The medium tray was actually very slightly negatively buoyant, and sank when placed upside down. The two long plates illustrate the subtle effect of shape with the second plate experiencing a larger drift enhancement factor despite similar relative size and geometry. This is a result of the first plate, which is somewhat smoother in shape, occasionally becoming submerged below the waves for a short time, reducing the drift. Although the aforementioned rigid objects generally remained floating, the nets, which are flexible and close to neutrally buoyant, all became submerged below the surface, traveling forwards at a much-reduced speed except for the most buoyant fine square net. This seems to suggest that there is a significant effect of density that only becomes important when objects are near-neutrally buoyant, such that they can be submerged into the water column by wave action.

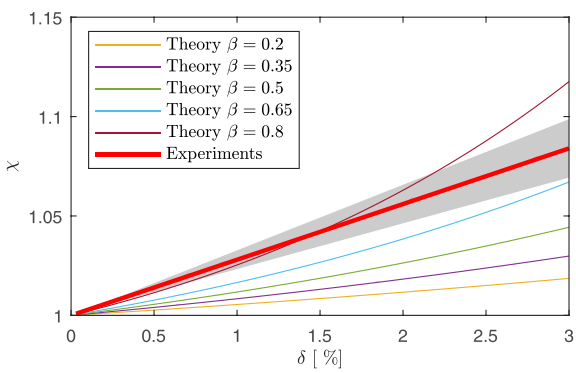

Figure 6. Comparison of experimental results for the drift enhancement factor of spheres with theoretical predictions by Calvert et al. (2021) (with relative densities $\beta = \rho_O/\rho_w = 0.2$–$0.8$). Eulerian-mean currents are eliminated from the experimental results using Method 2, and the shaded region covers one standard deviation either side of the mean.

4. Estimation of Drift for Floating Marine Litter in the Great Pacific Garbage Patch

In this section, we will examine the implications of our experimental findings for floating marine litter in wave conditions that are realistic for the Great Pacific Garbage Patch (GPGP) or the deep ocean more generally. Our experiments have shown that the main driver for increased wave-induced transport is object size relative to wavelength. The deep ocean is characterized by dominant wavelengths that are generally much larger than in our experiments, resulting in much smaller relative object size and thus much reduced drift enhancement in realistic ocean wave conditions compared to the

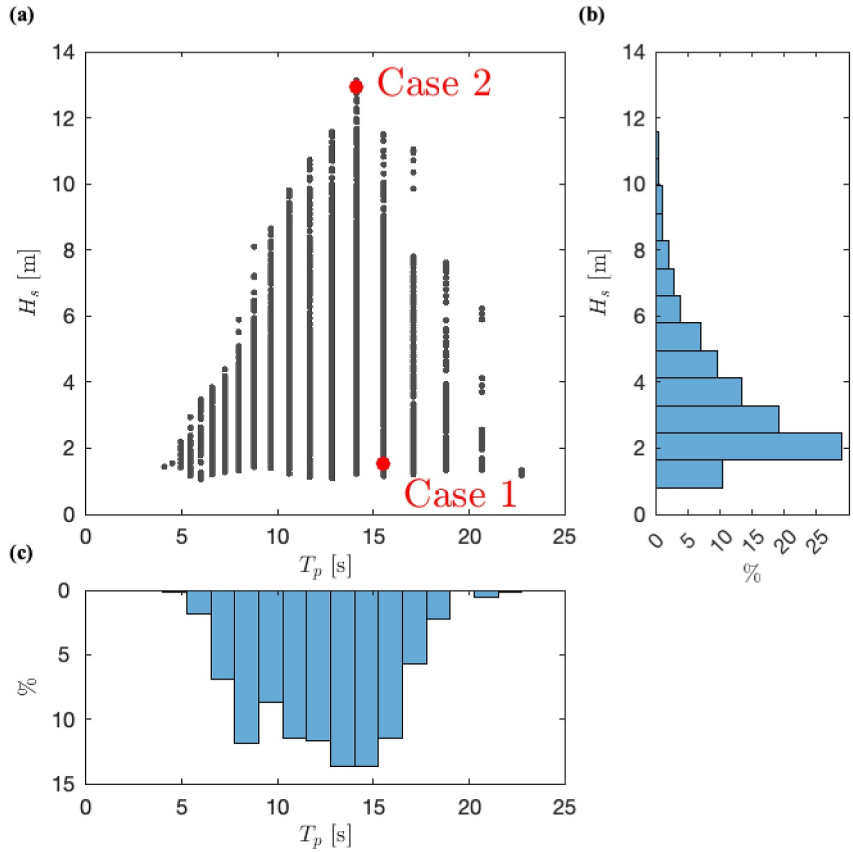

Figure 7. Histogram of significant wave height H_s and peak period T_p for 1 year of 1-hr wave spectra in the GPGP: (a) shows (T_p, H_s) for each 1-hr spectrum, and (b) and (c) show the histograms for H_s and T_p, respectively.

laboratory. Crucially, realistic wave conditions are irregular, that is, they are best represented by a spectrum of waves with different wavelengths. In such an irregular sea, it becomes unclear which wavelength to use in evaluating relative size, $\delta = D/\lambda$, in Equation 1. We will consider different approaches to this problem below.

4.1. Wave Conditions

We obtain spectra from a WaveWatch-III model of the North East Pacific (Tolman, 2009) at three locations inside the GPGP ([229.5°E, 42.6°N; 222.6°E, 40.8°N; 217.5°E, 30.5°N]). The WaveWatch-III implementation from which these spectra are extracted has previously been validated by comparing with wave buoys, unmanned surface vehicle motion derived wave characteristics and X-band radar measurements conducted during a field campaign in 2019 (Wrenger et al., 2012). Figure 7 shows a histogram of significant wave heights H_s and peak periods T_p during the 1-year period measured in the GPGP.

4.2. A Model for Estimating Drift Enhancement in Irregular Seas

To characterize realistic ocean wave conditions, we use 1-hr directional wave spectra we have modeled for the GPGP during a 1-year period. We will estimate the drift enhancement factor for all the 1-hr spectra during this 1-year period, which are then averaged over the 1-year period. The Stokes drift is computed from the energy spectrum $S(\omega)$ according to Kenyon (1969a):

$$u_S(z=0) = \int_{\omega_{\min}}^{\omega_{\max}} \underbrace{S(\omega)\frac{\omega^3}{g}}_{=\hat{u}_S|_{z=0}(\omega)} \mathrm{d}\omega, \tag{2}$$

where we have set $z = 0$, corresponding to the still-water level, and we have used the wavenumber and angular frequency limits set by the frequency limits of the modeled data ($\omega_{\min} = 0.25$ rad/s and $\omega_{\max} = 12.6$ rad/s corresponding to $f_{\min} = 0.04$ Hz and $f_{\max} = 2.0$ Hz).

We assume each spectral component of the Stokes drift, that is, $\hat{u}_S|_{z=0}(\omega) = S(\omega)\omega^3/g$, is independent, and these components can be summed together as in Equation 2 to obtain the Stokes drift, assumptions that are commonly made (Breivik, Bidlot, & Janssen, 2014; Kenyon, 1969b; Lenain & Pizzo, 2020; Webb & Fox-Kemper, 2011). In doing so, we have assumed that the entire spectrum consists of free waves, and bound waves do not play a role. Importantly, we note that Stokes drift (of non-breaking waves) may be underestimated significantly if the high-frequency tail is ignored (Lenain & Pizzo, 2020). The importance of the high-frequency spectral tail's contribution to the Stokes drift arises as a result of the multiplicative factor $k^{\frac{3}{2}}$ (or ω^3) in Equation 2. As finite-size objects have a larger relative size in shorter waves (larger k), the tail of the spectrum is potentially more important for their enhanced transport. Accordingly, we set out to estimate a spectrally weighted drift enhancement factor χ_{spec}.

Although our experiments were for monochromatic waves, we further assume that each spectral component of the Stokes drift $\hat{u}_S|_{z=0}(\omega)$ can be multiplied by its own drift enhancement factor $\chi(D, k(\omega))$ given by Equation 5, resulting in a spectral object drift component $\hat{u}_S|_{z=0}(\omega, D) = S(\omega)\omega^3/g\chi(D, k(\omega))$, which are then summed together. We thus define the spectrally weighted drift enhancement factor χ_{spec} as the object drift normalized by the Stokes drift (in the absence of Eulerian-mean flows):

$$\chi_{\text{spec}}(D) = \frac{\int_{\omega_{\min}}^{\omega_{\max}} \chi(D, k(\omega))\hat{u}_S(\omega)\mathrm{d}\omega}{\int_{\omega_{\min}}^{\omega_{\max}} \hat{u}_S(\omega)\mathrm{d}\omega}. \tag{3}$$

4.3. The Spectral Drift Enhancement Factor $\chi(D, k(\omega))$

To estimate the spectrally weighted drift enhancement factor χ_{spec} in Equation 3, we need to determine the spectral drift enhancement factor $\chi(D, k(\omega))$. Two limitations of our experiments need to be overcome. First, our experiments were for regular waves and not for a spectrum of irregular waves, for which it is not clear a priori that the independence assumption of spectral components underlying Equation 3 can be justified. Second, the range of relative sizes considered in our experiments does not cover the entire high-frequency tail of the Stokes drift spectrum, requiring extrapolation. We examine two approaches.

4.3.1. Approach 1: Based on Peak Frequency

Approach 1 calculates the drift enhancement based on a single frequency (and wavelength) representative of the peak of the spectrum (i.e., $\chi(D, k(\omega)) = \chi(D, k_p(\omega_p))$, so that χ can be taken outside of the integral in Equation 3 and the integrals in the numerator and the denominator become equal). A peak frequency ω_p can be extracted from each 1-hr spectrum, corresponding to a peak wavenumber k_p using the deep-water dispersion relation. The drift enhancement factor for Approach 1 becomes:

$$\chi_{\text{spec,A1}} = 1 + 5.6Dk_p/(2\pi), \tag{4}$$

where we have set the drift enhancement factor of an infinitely small object $\chi(D = 0) = \gamma_0 = 1$, so that such a particle is transported with the Stokes drift. We have used the value of $\gamma_\delta = 5.6$ for discs, as our data for discs covers a much larger range of relative sizes than for spheres. We have not included the effect of steepness, setting $\gamma_\epsilon = 0$.

If we take a sample of object sizes of 10, 50, and 100 cm representative of plastic larger plastic found in GPGP (Lebreton et al., 2018), we obtain average drift increases over the 1-year period of 0.3% (0.07%–2%), 1.6% (0.3%–10%), and 3.1% (0.7%–21%), where the values in brackets correspond to the 1-hr spectra during the 1-year period that gives the smallest and largest drift increases, respectively. It is evident that these increases are generally small, so small that they can be ignored, both on average over the 1-year period and in most 1-hr spectra, except for very large objects in a few very specific 1-hr spectra dominated by short waves.

4.3.2. Approach 2: Based on All Frequencies Independently

Approach 2 considers the drift enhancement of each frequency independently and sums the wave-induced drift from each frequency multiplied by a spectral drift enhancement factor (cf. Equation 3) based on our results for drift enhancement for the relative size $\delta = D/\lambda$ corresponding to that frequency. Specifically, we use

$$\chi_{A2}(\delta) = \begin{cases} 1 + 5.6\delta & \text{if } \delta \le 0.128, \\ \begin{cases} 1 + 5.6\delta & \text{Approach a} \\ 1.73 & \text{Approach b} \\ 1.73 - 5.6(\delta - 0.128) \text{ for } \delta < 0.256, 1 \text{ for } \delta > 0.256 & \text{Approach c} \\ 1 & \text{Approach d} \end{cases} & \text{if } \delta > 0.128, \end{cases} \quad (5)$$

where we consider four different approaches (a–d) to extrapolating $\chi(\delta)$ to large relative sizes for which we do not have measurements (restricted by possible wave frequencies generated by the wavemaker and object sizes available in the experiments), namely for ($\delta > 0.128$): (a) continuation of the linear trend, (b) a constant value of $\chi = 1.73$ at the largest constant value we have measured, (c) a linear decrease of χ with δ back to zero with the same absolute slope, and (d) a constant value of $\chi = 1$. Figure 8 illustrates this by showing Equation 5 as a function of ω (for a $D = 50$ cm object), as this facilitates inclusion into Equation 3. Going from Approach 2a to 2d, the extrapolations used include less and less drift enhancement. Although we don't observe this in our experiments, the drift enhancement must stop increasing with relative size at large enough relative size. We understand neither the mechanism that would cause this nor the relative size at which it would occur. Our approach to this uncertainty in the present paper has been to adopt the above four different extrapolation techniques: 2a assumes this unknown limit is very far away from the range of our experiments, 2d that it occurs exactly at the end of our experimental range. We begin by examining Approach 2b as our base case.

4.4. Wave and (Enhanced) Stokes Drift Spectra (Approach 2b)

Figures 9a and 9c show the modeled energy spectra $S(\omega)$ for the two cases shown in Figure 7 as Case 1 and Case 2, chosen as those 1-hr spectra that give rise to the largest and the smallest total drift enhancement. Also shown for comparison are JONSWAP spectra fitted to the modeled spectra using least squares. Case 2 is represented well by a JONSWAP spectrum, whereas Case 1 has a much more complex tail, and the spectrum is potentially bi-modal. Both the energy spectrum $S(\omega)$ (left vertical axes) and the drift enhancement factor $\chi(\omega)$ for $D = 10$, 50 and 100 cm (right vertical axes) are shown in Figures 9a and 9c for Cases 1 and 2.

Figures 9b and 9d show both the spectral components of the Stokes drift, $\hat{u}_S|_{z=0}(\omega) = S(\omega)\omega^3/g$, and of the enhanced object drift, $\chi(D,\omega)\hat{u}_S|_{z=0}(\omega)$, as a function of angular frequency ω for the three different object sizes ($D = 10$, 50, and 100 cm). Comparing the energy spectra in Figures 9a and 9c with the Stokes drift spectra in Figures 9b and 9d confirms the tail of the spectrum makes a large contribution to the Stokes drift (cf. Lenain & Pizzo, 2020) (N.B. the logarithmic vertical axes). When relative size of the objects is taken into account (using Approach 2b, cf. (cf. Equation 5), the effect of the tail becomes even larger). The spectrally weighted drift enhancements factors χ_{spec} for the three different object sizes are shown in Figures 9b and 9d. It is immediately evident that the case with the most pronounced spectral tail (Case 1) results in the largest drift enhancement.

Evaluating the integrals in Equation 3 for all the 1-hr spectra for the GPGP during a 1-year period, we predict average (minimum-maximum) increases in drift (i.e., $(\chi_{spec,A2b} - 1) \times 100\%$) of 3% (2%–6%), 27% (18%–47%), 51% (36%–68%), and 59% (43%–70%) for 1, 10, 50, and 100 cm diameters, respectively, as shown in Table 5. The strong effect of object size is evident, with 1 cm objects experiencing a negligibly small increase in drift but 100 cm objects experiencing a very substantial increase.

From Figures 9b and 9d the importance of the spectral tail and its short waves with large spectral drift enhancement factors (truncated at 1.73) is clear, which we examine further by varying the frequency upper limit ω_{max}. The integrals over frequency for the Stokes drift Equation 4 and the wave-induced object drift (numerator of

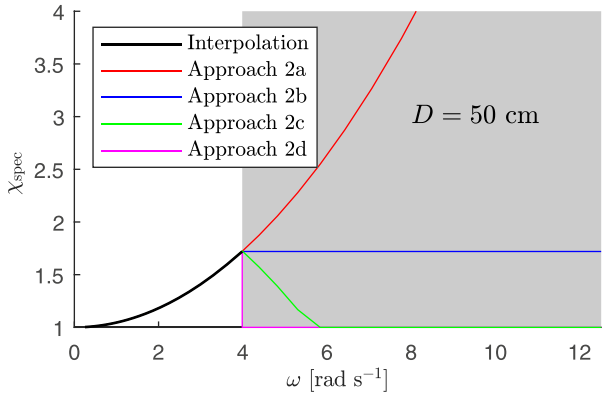

Figure 8. Different extrapolation techniques used to extend the spectral drift enhancement factor beyond measured values (interpolation, black line) to the extrapolation region (gray) for a $D = 50$ cm object for the spectral frequency range measured in the GPGP.

Equation 5) can be evaluated with different upper limits ω_{max}, resulting in the spectral tail playing a more or less important role. Similar to results found in Lenain and Pizzo (2020), the spectral tail has a significant contribution to the Stokes drift, as shown in the left panels of Figure 10, where the value of the (total) Stokes drift decays quickly when the upper limit ω_{max} is reduced. This can also be seen in the spectrally weighted drift enhancement factor $\chi_{spec,\ A2b}$ for the three finite-size objects in the right panels of Figure 10. The spectral tail has shorter wavelengths and so higher drift enhancements factors for larger objects. Although the tail contributes the most to any enhanced wave-induced object drift, there is an increase in drift for larger objects for even low values of the upper limit. The reason the values of $\chi_{spec\ A2b}$ begin to saturate for higher values of ω_{max} is the truncation of our drift enhancement factor χ to a maximum value of 1.73 for values of relative size above what we have measured in our experiments in extrapolation Approach 2b.

4.5. Comparing the Different Extrapolation Approaches

Table 6 shows that all four extrapolation methods predict an increase in wave-induced drift, but that the magnitude of the enhancement predicted depends significantly on the extrapolation approach taken. For example, the maximum increase for an 100 cm floating marine litter object varies between 590% and 14% depending on whether Approach 2d or 2a is used, where we note that these two methods probably cover the range of what is possible in reality. Furthermore, we note that these predictions are based on experiments for disc-shaped objects, which displayed the greatest drift of all objects we considered in our experiments. Nevertheless, we conclude from Table 6 that large objects will likely experience an appreciable increase in drift compared to their Lagrangian counterparts in realistic wave conditions. For

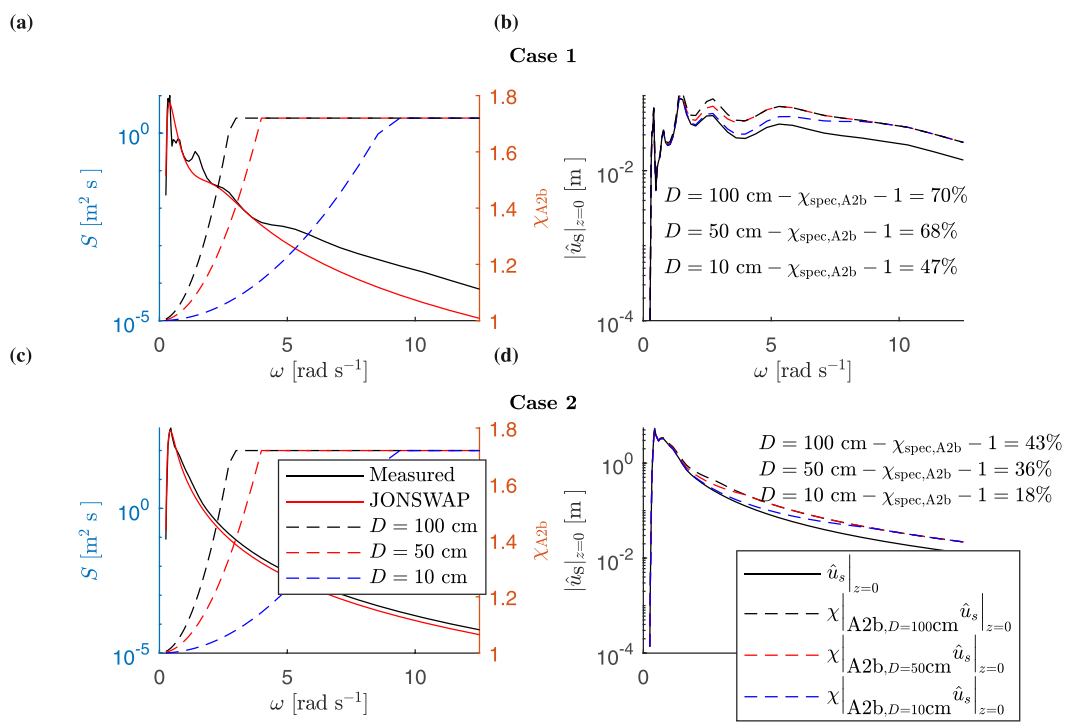

Figure 9. Two 1-hr wave energy spectra and corresponding (enhanced) Stokes drift spectra for the Great Pacific Garbage Patch, showing Case 1 (top row) and Case 2 (bottom row) as defined in Figure 7: (a, c) modeled energy spectra and fitted JONSWAP spectra $S(\omega)$ (left axis) and spectral drift enhancement factors $\chi_{A2b}(D, \omega)$ for $D = 10$, 50 and 100 cm (right axis) using Approach 2b (cf. Equation 5)); (b, d) Stokes drift spectra, $\hat{u}_S|_{z=0}(\omega)$, and enhanced Stokes drift spectra, $\chi_{A2b}(D,\omega)\hat{u}_S|_{z=0}(\omega)$, also showing the values of the resulting spectrally weighted drift enhancements factors $\chi_{spec,\ A2b}$ for $D = 10$, 50 and 100 cm.

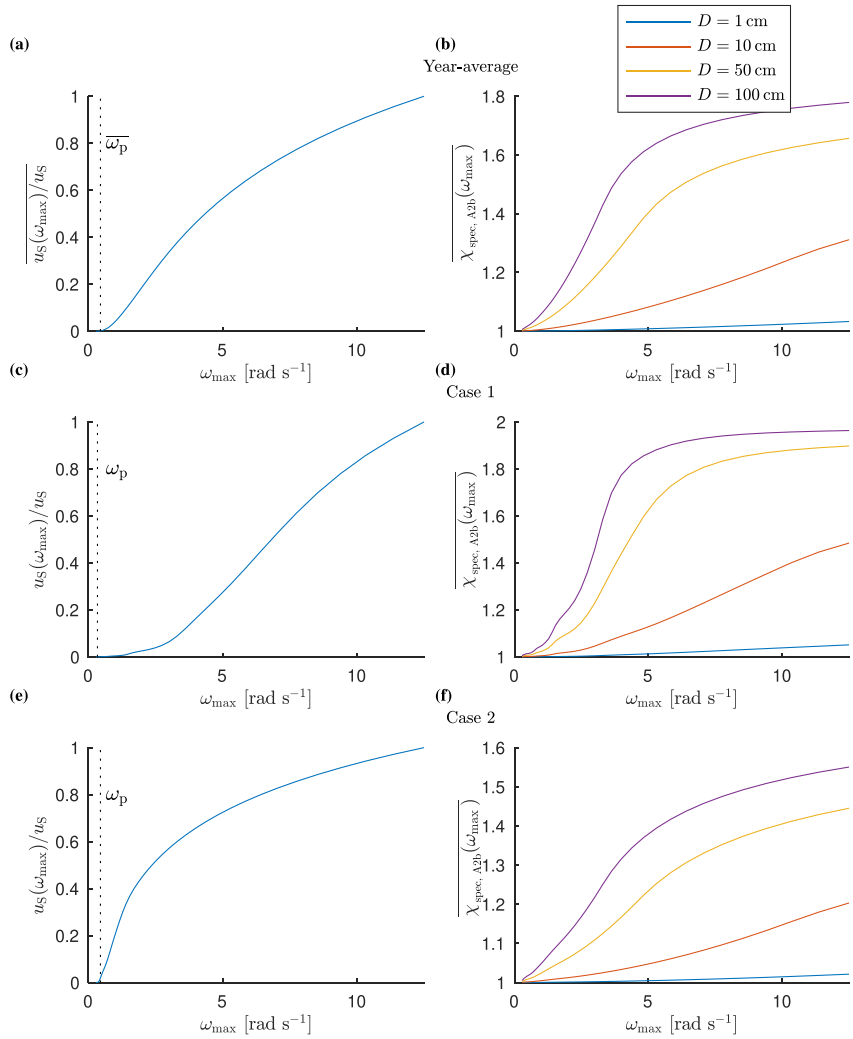

Figure 10. Effect of changing the frequency upper limit ω_{max} on the Stokes drift (left) and on the spectrally weighted drift enhancement factor $\chi_{spec,\,A2b}$ (right) for the 1-year averaged (top), case 1 (middle) and case 2 (bottom) wave conditions. The Stokes drift $u_S(\omega_{max})$ as a function of its frequency upper limit ω_{max} is normalized by the Stokes drift u_S corresponding to the maximum value of the upper limit (i.e., $\omega_{max} = 2.0 \times 2\pi$ rad/s). The effect of the upper limit is shown on the right by calculating the spectrally weighted drift enhancement factor χ_{spec} as a function of ω_{max} using extrapolation Approach 2b.

Table 6
Effect of the Different Extrapolation Approaches (1, 2a–2d) on the Predicted Spectrally Weighted Drift Enhancements ($(\chi_{spec} - 1) \times 100\%$) for Floating Marine Litter Objects With Different Sizes Averaged Over a 1-Year Period and With Values in Brackets Showing the 1-Hour Spectra Within This Period With Minimum and Maximum Drift Enhancements

Extrapolation Approach	1 cm	10 cm	50 cm	100 cm
1	0.03% (0.01%–0.3%)	0.3% (0.07%–2%)	1.6% (0.3%–10%)	3.1% (0.7%–21%)
2a	3.2% (2.1%–6.0%)	27% (21%–59%)	164% (110%–300%)	320% (210%–590%)
2b	3.2% (2.1%–6.0%)	27% (18%–47%)	51% (36%–68%)	59% (43%–70%)
2c	3.2% (2.1%–6.0%)	23% (15%–36%)	19% (9.6%–23%)	116% (4.5%–20%)
2d	3.2% (2.1%–6.0%)	16% (11%–14%)	11% (3.6%–14%)	10% (2.1%–14%)

Note. There is no extrapolation applied to a 1 cm object.

context, we note that although mega-plastic, defined as objects greater than 50 cm in size, had the lowest count of any size class collected from the GPGP, it accounted for over 60% of the mass of plastic collected (Lebreton et al., 2018). We note that to enable comparison with potential field measurements of drift of objects with different sizes, both the effects identified in the present paper and the effects of directional spreading (Webb & Fox-Kemper, 2015), Coriolis forces (Cunningham et al., 2022; Higgins et al., 2020), and wave breaking (Deike et al., 2017; Eeltink et al., 2023; Lenain et al., 2019; Sinnis et al., 2021) should be taken into account.

5. Conclusions

Large-scale laboratory flume experiments have been used to examine how the surface wave-induced drift of floating marine litter objects of finite size depends on their size, density and shape. Our results are only valid for deep-water waves ($kd > 3$) and thus apply directly to coastal but only indirectly to nearshore conditions. In these experiments, we have systematically varied the size and density of idealized objects (spheres and discs) and also examined realistic marine litter with often complex shapes. Although wave-induced Eulerian-mean flows have often prevented observation of Stokes drift in laboratory wave flumes (Monismith, 2020; Monismith et al., 2007; van den Bremer & Breivik, 2017), we have corrected for their effect, by simultaneously measuring the Eulerian current and by always considering the drift of larger objects compared to the drift of very small objects.

We observe increases in drift of 95% compared to Stokes drift for discs with diameters of 13% of the wavelength and up to 23% for spheres with diameters of 3% of the wavelength (the smallest objects we consider). A linear regression analysis of the drift enhancement factor on object size relative to wavelength, object density and wave steepness, shows a clear linear dependence of the drift enhancement factor on relative size. As a rule of thumb, the drift enhancement factor goes up by 3% points for spheres and by 5%–6% points for discs when their relative sizes go up by 1% point. Discs are thus generally transported faster than spheres. For spheres, this experimental finding agrees reasonably well with the theoretical prediction by Calvert et al. (2021), although the role of object density deserves further attention (the theoretical model of Calvert et al. (2021) only considered spheres). We do not find a significant effect of density for the idealized objects, where $\beta < 0.92$. Finally, we do find a significant positive linear dependence of the drift enhancement factor on the steepness, suggesting that breaking increases the wave-induced drift compared to the Stokes drift, as found by Deike et al. (2017), Lenain et al. (2019), and Sinnis et al. (2021), although we have not examined this in sufficient detail to draw firm conclusions. Rigid floating marine litter objects also experience an increased drift, and the drift enhancement is of a comparable magnitude to discs of similar size. On the contrary, fishing nets, which can deform and are close to neutrally buoyant (*beta* 1), do not stay afloat in a wave field, but become submerged below the surface, traveling forwards at a much-reduced speed compared to the Stokes drift.

The size-enhanced wave-induced drift of floating marine litter we have observed in our experiments depends crucially on the size of the objects not being too small relative to the wavelength. Noting that the high-frequency tail of the spectrum makes a large contribution to the Stokes drift (Lenain & Pizzo, 2020) and an even larger contribution to size enhanced wave-induced drift, we have estimated the drift enhancement for modeled wave spectra in the Great Pacific Garbage Patch. These results depend strongly on the amount of energy present in the tail of the wave spectrum and its contribution to the Stokes drift. Individual wave components in the spectral tail will result in large relative object sizes for that spectral component alone, beyond the range we have studied experimentally, for which our linear relationship between the drift enhancement factor and relative size will likely become invalid. Different extrapolations have been examined, all of which show an increase in wave-induced drift, but whose magnitude depends very strongly on the approach to extrapolation taken. Future experiments should examine this, not only by conducting experiments with monochromatic waves for larger relative object sizes, but also by considering irregular waves based on a spectrum with a realistic tail, so that the validity of linear superposition of (enhanced) drift components can be interrogated.

We have not examined or considered the effect of surface tension in this paper. We propose this is a reasonable approximation for floating objects provided their diameter $D > 2\sqrt{\gamma/(\rho g)}$, where γ is the surface tension, ρ the density of water and g the gravitational acceleration (e.g., Falkovich et al., 2005). For water, this criterion is satisfied for objects of diameters exceeding 5 mm, resulting in the findings of this paper being invalid for micro-plastic objects. However, such small objects are unlikely to experience drift enhancement due to the effect examined herein (N.B. our smallest object has a 20 mm diamater). We can thus conclude that the regime in which

Table A1
Expanded Version of Table 2 Giving Description, Shape and Parameter Range for the Idealized Objects (Category I)

No.	Picture	Description and shape	D (mm)	ρ_O (kg/m^3)
1–15		Spheres	20–50	195–920
1		Sphere	20	395
2		Sphere	38	260
3		Sphere	50	196
4		Sphere	17	689
5		Sphere	40	472
6		Sphere	50	504
7		Sphere	20	477
8		Sphere	38	652
9		Sphere	50	611
10		Sphere	20	716
11		Sphere	38	766
12		Sphere	49	797
13		Sphere	19	920
14		Sphere	38	920
15		Sphere	48	920
16–19		Discs	50–200	750–880
16		Disc	50	878
17		Disc	99	806
18		Disc	149	818
19		Disc	200	753

surface tension is important and the regime in which significant drift enhancement occurs, as observed in this paper, are likely mutually exclusive.

Separately, we have not examined the thin (viscous) wave-driven surface boundary layer that can form in the laboratory and the field and takes the form of a strongly sheared Eulerian-mean flow that is in the direction of the waves, thus enhancing Lagrangian-mean transport. This so-called boundary layer streaming (Longuet-Higgins, 1953) can be significant in large-steepness waves (Grue & Kolaas, 2017). It is conceivable that different floating objects could penetrate a different distance into the (thin) surface boundary layer, and this could be a cause of differential contributions of boundary layer streaming to the drift of different objects and the properties of the boundary layer (namely Reynolds number and thus the scale of experiments) becoming important. Future work should examine this.

We foresee that the size-enhanced wave-induced drift we have identified will result in the wave-driven transport due to Stokes drift being more important than previously thought in studies of global marine litter transport, especially of macro-plastic. It may lead to a sorting of plastic by size, which may be further enhanced by wind drag. Size-enhanced wave-induced drift may be even more important in the coastal zones, where shorter wavelengths are dominant. In future work, experiments with irregular and directionally spread waves based on realistic spectra should be carried out to verify our predictions, although we emphasize that such experiments should be carried out at a scale as large as possible, as the mechanism for drift enhancement may depend on the drag the waves exerts on the objects (Calvert et al., 2021) and thus on Reynolds and Stokes numbers (Sutherland et al., 2023).

Appendix A: Detailed Table of Idealized Object Properties (Category I)

Table A1 gives provides a list of the properties of the Idealized Objects (Category I).

Data Availability Statement

The data used in this paper can be accessed at https://figshare.com/s/cfda63f7c09e300388a5?file=35129710 which can be accessed under the Creative Commons license.

Acknowledgments
The experiments reported on in this paper were funded by the Ocean Cleanup Foundation. TSvdB acknowledges support from a Royal Academy of Engineering Research Fellowship.

References

Alsina, J. M., Jongedijk, C. E., & van Sebille, E. (2020). Laboratory measurements of the wave-induced motion of plastic particles: Influence of wave period, plastic size and plastic density. *Journal of Geophysical Research: Oceans*, *125*(12), e2020JC016294. https://doi.org/10.1029/2020jc016294

Breivik, O., Bidlot, J., & Janssen, P. A. E. M. (2014). Approximate Stokes drift profiles in deep water. *Journal of Physical Oceanography*, *44*(9), 2433–2445. https://doi.org/10.1175/jpo-d-14-0020.1

Breivik, O., Janssen, P., & Bidlot, J.-R. (2014). Approximate Stokes drift profiles in deep water. *Journal of Physical Oceanography*, *44*(9), 2433–2445. https://doi.org/10.1175/JPO-D-14-0020.1

Bühler, O. (2014). *Waves and mean flows* (2nd ed.). Cambridge University Press.

Calvert, R., McAllister, M., Whittaker, C., Raby, A., Borthwick, A., & van den Bremer, T. (2021). A mechanism for the increased wave-induced drift of floating marine litter. *Journal of Fluid Mechanics*, *925*, A73. https://doi.org/10.1017/jfm.2021.72

Cózar, A., Echevarría, F., González-Gordillo, J. I., Irigoien, X., Úbeda, M., Hernández-León, S., et al. (2014). Plastic debris in the open ocean. *Science*, *111*(28), 10239–10244. https://doi.org/10.1073/pnas.1314705111

Cunningham, H. J., Higgins, C., & van den Bremer, T. (2022). The role of the unsteady surface wave-driven Ekman–Stokes flow in the accumulation of floating marine litter. *Journal of Geophysical Research: Oceans*, *127*(6), e2021JC01810. https://doi.org/10.1029/2021jc018106

Deike, L., Pizzo, N., & Melville, W. K. (2017). Lagrangian transport by breaking surface waves. *Journal of Fluid Mechanics*, *829*, 364–391. https://doi.org/10.1017/jfm.2017.548

Delandmeter, P., & van Sebille, E. (2019). The parcels v2.0 Lagrangian framework: New field interpolation schemes. *Geoscientific Model Development*, *12*(8), 3571–3584. https://doi.org/10.5194/gmd-12-3571-2019

DiBenedetto, M. H., Clark, L. K., & Pujara, N. (2022). Enhanced settling and dispersion of inertial particles in surface waves. *Journal of Fluid Mechanics*, *936*, A38. https://doi.org/10.1017/jfm.2022.95

DiBenedetto, M. H., Koseff, J. R., & Ouellette, N. T. (2019). Orientation dynamics of nonspherical particles under surface gravity waves. *Physical Review Fluids*, *4*(3), 034301. https://doi.org/10.1103/physrevfluids.4.034301
DiBenedetto, M. H., & Ouellette, N. T. (2018). Preferential orientation of spheroidal particles in wavy flow. *Journal of Fluid Mechanics*, *856*, 850–869. https://doi.org/10.1017/jfm.2018.738
DiBenedetto, M. H., Ouellette, N. T., & Koseff, J. R. (2018). Transport of anisotropic particles under waves. *Journal of Fluid Mechanics*, *837*, 320–340. https://doi.org/10.1017/jfm.2017.853
Dobler, D., Huck, T., Maes, C., Grima, N., Blanke, B., Martinez, E., & Ardhuin, F. (2019). Large impact of Stokes drift on the fate of surface floating debris in the South Indian Basin. *Marine Pollution Bulletin*, *148*, 202–209. https://doi.org/10.1016/j.marpolbul.2019.07.057
Eames, I. (2008). Settling of particles beneath water waves. *Journal of Physical Oceanography*, *38*(12), 2846–2853. https://doi.org/10.1175/2008jpo3793.1
Eeltink, D., Calvert, R., Swagemakers, J., Xiao, Q., & van den Bremer, T. (2023). Stochastic particle transport by deep-water irregular breaking waves. *Journal of Fluid Mechanics*, *971*, A38. https://doi.org/10.1017/jfm.2023.671
Eriksen, M., Lebreton, L. C. M., Carson, H. S., Thiel, M., Moore, C. J., Borerro, J. C., et al. (2014). Plastic pollution in the world's oceans: More than 5 trillion plastic pieces weighing over 250,000 tons afloat at sea. *PLoS One*, *9*(12), e111913. https://doi.org/10.1371/journal.pone.0111913
Falkovich, G., Weinberg, A., Denissenko, P., & Lukaschuk, S. (2005). Floater clustering in a standing wave. *Nature*, *435*(7045), 1045–1046. https://doi.org/10.1038/4351045a
Fraser, C., Morrison, A., Hogg, A. M., Macaya, E., van Sebille, E., Ryan, P., et al. (2018). Antarctica's ecological isolation will be broken by storm-driven dispersal and warming. *Nature Climate Change*, *8*(8), 704–708. https://doi.org/10.1038/s41558-018-0209-7
Geyer, R., Jambeck, J. R., & Lavender Law, K. (2017). Production, use, and fate of all plastics ever made. *Science Advances*, *3*(7), e1700782. https://doi.org/10.1126/sciadv.1700782
Goldstein, M. C., Rosenberg, M., & Cheng, L. (2012). Increased oceanic microplastic debris enhances oviposition in an endemic pelagic insect. *Biology Letters*, *8*(5), 817–820. https://doi.org/10.1098/rsbl.2012.0298
Grue, J., & Kolaas, J. (2017). Experimental particle paths and drift velocity in steep waves at finite water depth. *Journal of Fluid Mechanics*, *810*, R1. https://doi.org/10.1017/jfm.2016.726
Higgins, C., Vanneste, J., & van den Bremer, T. S. (2020). Unsteady Ekman-Stokes dynamics: Implications for surface wave-induced drift of floating marine litter. *Geophysical Research Letters*, *47*(18), e2020GL089189. https://doi.org/10.1029/2020gl089189
Huang, G., Huang, Z. H., & Law, A. W. K. (2016). Analytical study on drift of small floating objects under regular waves. *Journal of Engineering Mechanics*, *142*(6), 06016002. https://doi.org/10.1061/(ASCE)EM.1943-7889.0001067
Iwasaki, S., Isobe, A., Kako, S., Uchida, K., & Tokai, T. (2017). Fate of microplastics and mesoplastics carried by surface currents and wind waves: A numerical model approach in the Sea of Japan. *Marine Pollution Bulletin*, *121*(1), 85–96. https://doi.org/10.1016/j.marpolbul.2017.05.057
Jambeck, J. R., Geyer, R., Wilcox, C., Siegler, T. R., Perryman, M., Andrady, A., et al. (2015). Plastic waste inputs from land into the ocean. *Science*, *347*(6223), 768–771. https://doi.org/10.1126/science.1260352
Kaandorp, M. L., Lobelle, D., Kehl, C., Dijkstra, H. A., & van Sebille, E. (2023). Global mass of buoyant marine plastics dominated by large long-lived debris. *Nature Geoscience*, *16*(8), 1–6. https://doi.org/10.1038/s41561-023-01216-0
Kenyon, K. E. (1969a). Stokes drift for random gravity waves. *Journal of Geophysical Research*, *74*(28), 6991–6994. https://doi.org/10.1029/JC074i028p06991
Kenyon, K. E. (1969b). Stokes drift for random gravity waves. *Journal of Geophysical Research*, *74*(28), 6991–6994. https://doi.org/10.1029/JC074i028p06991
Lavender Law, K. (2017). Plastics in the marine environment. *Annual Review of Marine Science*, *9*(1), 205–229. https://doi.org/10.1146/annurev-marine-010816-060409
Lebreton, L., Egger, M., & Slat, B. (2019). A global mass budget for positively buoyant macroplastic debris in the ocean. *Scientific Reports*, *9*(1), 12922. https://doi.org/10.1038/s41598-019-49413-5
Lebreton, L., Slat, B., Ferrari, F., Sainte-Rose, B., Aitken, J., Marthouse, R., et al. (2018). Evidence that the Great Pacific Garbage Patch is rapidly accumulating plastic. *Scientific Reports*, *8*(1), 4666. https://doi.org/10.1038/s41598-018-22939-w
Lenain, L., & Pizzo, N. (2020). The contribution of high-frequency wind-generated surface waves to the Stokes drift. *Journal of Physical Oceanography*, *50*(12), 3455–3465. https://doi.org/10.1175/jpo-d-20-0116.1
Lenain, L., Pizzo, N., & Melville, W. K. (2019). Laboratory studies of Lagrangian transport by breaking surface waves. *Journal of Fluid Mechanics*, *876*, R1. https://doi.org/10.1017/jfm.2019.544
Longuet-Higgins, M. S. (1953). Mass transport in water waves. *Philosophical Transactions of the Royal Society of London—A*, *245*(903), 535–581. https://doi.org/10.1098/rsta.1953.0006
Lukezic, A., Vojir, T., Cehovin Zajc, L., Matas, J., & Kristan, M. (2017). Discriminative correlation filter with channel and spatial reliability. In *Proceedings of the IEEE conference on computer vision and pattern recognition* (pp. 6309–6318).
Maxey, M. R., & Riley, J. J. (1983). Equation of motion for a small rigid sphere in a non-uniform flow. *Physics of Fluids*, *26*(4), 883–889. https://doi.org/10.1063/1.864230
Monismith, S. G. (2020). Stokes drift: Theory and experiments. *Journal of Fluid Mechanics*, *884*, F1. https://doi.org/10.1017/jfm.2019.891
Monismith, S. G., Cowen, E., Nepf, H. M., Magnaudet, J., & Thais, L. (2007). Laboratory observations of mean flows under surface gravity waves. *Journal of Fluid Mechanics*, *573*, 131–147. https://doi.org/10.1017/s0022112006003594
Onink, V., Wichmann, D., Delandmeter, P., & van Sebille, E. (2019). The role of Ekman currents, geostrophy, and Stokes drift in the accumulation of floating microplastic. *Journal of Geophysical Research: Oceans*, *124*(3), 1474–1490. https://doi.org/10.1029/2018JC014547
Ostle, C., Thompson, R., Broughton, D., Gregory, L., Wootton, M., & Johns, D. G. (2019). The rise in ocean plastics evidenced from a 60-year time series. *Nature Communications*, *10*(1), 1622. https://doi.org/10.1038/s41467-019-09506-1
Pizzo, N., Melville, W. K., & Deike, L. (2019). Lagrangian transport by nonbreaking and breaking deep-water waves at the ocean surface. *Journal of Physical Oceanography*, *49*(4), 983–992. https://doi.org/10.1175/jpo-d-18-0227.1
Pujara, N., & Thiffeault, J.-L. (2023). Wave-averaged motion of small particles in surface gravity waves: Effect of particle shape on orientation, drift, and dispersion. *Physical Review Fluids*, *8*(7), 074801. https://doi.org/10.1103/PhysRevFluids.8.074801
Santamaria, F., Boffetta, F., Martins Afonso, M., Mazzino, A., Onorato, M., & Pugliese, D. (2013). Stokes drift for inertial particles transported by water waves. *Europhysics Letters*, *102*(1), 14003. https://doi.org/10.1209/0295-5075/102/14003
Sinnis, J. T., Grare, L., Lenain, L., & Pizzo, N. (2021). Laboratory studies of the role of bandwidth in surface transport and energy dissipation of deep-water breaking waves. *Journal of Fluid Mechanics*, *927*, A5. https://doi.org/10.1017/jfm.2021.734
Stokes, G. G. (1847). On the theory of oscillatory waves. *Transaction of the Cambridge Philosophical Society*, *8*, 441–455.

Sutherland, B. R., DiBenedetto, M., Kaminski, A., & van den Bremer, T. S. (2023). Fluid dynamics challenges in predicting plastic pollution transport in the ocean: A perspective. *Physical Review Fluids*, *8*(7), 070701. https://doi.org/10.1103/PhysRevFluids.8.070701

The WAMDI Group. (1988). The WAM model-A third generation ocean wave prediction model. *Journal of Physical Oceanography*, *18*(12), 1775–1810. https://doi.org/10.1175/1520-0485(1988)018⟨1775:TWMTGO⟩2.0.CO;2

Tolman, H. L. (2009). User manual and system documentation of WAVEWATCH III TM version 3.14 Technical Note.

van den Bremer, T. S., & Breivik, Ø. (2017). Stokes drift. *Philosophical Transactions of the Royal Society of London—A*, *376*(2111), 20170104. https://doi.org/10.1098/rsta.2017.0104

van Sebille, E., Aliani, S., Law, K. L., Maximenko, N., Alsina, J., A. Bagaev, M. B., et al. (2020). The physical oceanography of the transport of floating marine debris. *Environmental Research Letters*, *15*(2), 023003. https://doi.org/10.1088/1748-9326/ab6d7d

van Sebille, E., Wilcox, C., Lebreton, L., Maximenko, N., Hardesty, B. D., van Franeker, J. A., et al. (2015). A global inventory of small floating plastic debris. *Environmental Research Letters*, *10*(12), 124006. https://doi.org/10.1088/1748-9326/10/12/124006

Webb, A., & Fox-Kemper, B. (2011). Wave spectral moments and Stokes drift estimation. *Ocean Modelling*, *40*(3), 273–288. https://doi.org/10.1016/j.ocemod.2011.08.007

Webb, A., & Fox-Kemper, B. (2015). Impacts of wave spreading and multidirectional waves on estimating Stokes drift. *Ocean Modelling*, *96*, 49–64. https://doi.org/10.1016/j.ocemod.2014.12.007

Wilcox, C., Hardesty, B. D., & K, L. L. (2020). Abundance of floating plastic particles is increasing in the western North Atlantic Ocean. *Environmental Science & Technology*, *54*(2), 790–796. https://doi.org/10.1021/acs.est.9b04812

Wrenger, H., Sainte-Rose, B., & Soares, I. (2012). *Waves in the Great Pacific Garbage Patch: Cross validation of three measurement techniques and two WW3 models*. OMAE. 18891.

Xiao, Q., Calvert, R., Yan, S., Adcock, T., & van den Bremer, T. (2024). Surface gravity wave-induced drift of floating objects in the diffraction regime. *Journal of Fluid Mechanics*, *980*, A27. https://doi.org/10.1017/jfm.2024.31

Zhang, Z. (2000). A flexible new technique for camera calibration. *EEE Transactions on Pattern Analysis and Machine Intelligence*, *22*(11), 1330–1334. https://doi.org/10.1109/34.888718